Microstructure and *in vitro* Bioactivity of Metal Substituted Hydroxyapatite

G. El-Damrawi[1], H. Kamal[1,2*], H. Doweidar[1] and A. E. Dawood[1]

[1]*Department of Physics, Faculty of Science, Mansoura University, Mansoura, 35516, Egypt.*
[2]*Department of Medical Laboratories, Faculty of Applied Medical Sciences, Al-Jouf University, Al-Qurayyat, Saudi Arabia.*

Authors' contributions

This work was carried out in collaboration between all authors. Authors GED and HK designed the study, performed the statistical analysis, wrote the protocol, wrote the first draft of the manuscript and managed literature searches. Author AED managed the analyses of the study and literature searches. All authors read and approved the final manuscript.

Original Research Article

ABSTRACT

Pure Hydroxyapatite (HAp) nanoparticles doped with Mn^{2+} and Fe^{3+} ions were synthesized using wet chemical method (WCM). Samples were characterized by different spectroscopic techniques such as XRD, FTIR, and ESR. The measurements revealed that a typical HAp powder pattern was obtained. Comparing with pure stoichiometric HAp, both Mn^{+2} substituted HAp (Mn-HAp) and Fe^{+3} substituted HAp (Fe-HAp) did not demonstrate significant structure deviation. Since ion exchange mechanism was applied for the preparation process, the morphology and particle size were not significantly affected. The FTIR absorption spectra of the doped samples are presented as absorption bands characterizing $Mn^{+2,}$ and Fe^{+3} which occupy different crystalline sites. The obtained data agrees well with that obtained from XRD. The crystal field parameters and degree of crystallinity for sites of these ions in the HAp matrix can be estimated. The addition of iron and manganese ions into hydroxyapatite results in improvement of the biological performance of the implant. Iron and manganese substituted hydroxyapatite has shown superior biological performance compared to its stoichiometric counterparts in vitro. The addition of such ions also enhances the magnetic properties of hydroxyapatite for the use in hyperthermia medical applications.

_____

Corresponding author: E-mail: hkamal2000@yahoo.com, hkelsayed@ju.edu.sa;

1. INTRODUCTION

Development of new materials is considered to be one of the most important objectives of biomaterials science for bone substitution. Hydroxyapatite (HAp) {$Ca_{10}(PO_4)_6(OH)_2$} is one of the important biominerals of interest in the broad group of calcium phosphate based bioceramics and the main inorganic constituent of bone and teeth. HAp is mainly used as bone and dental replacement material. Hydroxapatite is reported to be fully non-resorbable when tested *in vivo* [1-3].

The major advantage of hydroxyapatite phase of calcium phosphate materials is that the nano size (10–100 nm) hydroxyapatite crystalline arrays along the collagen fibers inside the bone is able to bond directly with the hard tissue and can provide perfect lattice matching between the fracture bone surfaces. Moreover, HAp exhibits osteoconductive behavior, is stable toward bioresorption, and has no adverse effects on the human organism.

Hydroxyapatite (HAp) is the main inorganic phase of human bones and teeth [1-3]. Its structure is nearly similar to natural bone material which consists of nearly 72 wt% apatitic materials. Calcium to phosphate ratio (Ca/P) in the building structure of HAp is 1.67. This ratio is very close to the Ca/P of natural bone [4,5]. Hydroxyapatites have a wide range of applications both in medicine and dentistry due to the same characteristic properties [6,7]. The most important characteristic properties of HAps are good bioactivity and biocompatibility. The biocompatibility property comes from the non toxic effects on human tissues [8,9]. Implants coated with HAps promote a direct physiochemical bond with bone, which leads to more rapid implant fixation and the development of a stable bone biomaterial interface [10].

The main disadvantage of HAp is that they cannot be applicable to use for heavy load bearing applications due to its low mechanical properties in wet environments. In addition, HAp can be dissolved directly during its setting in living tissues. The problems associated with rapid dissolution, fatigue failure and the creation of particulate debris can be solved by addition of some types of reinforced agent such as iron oxide and Mn oxides to Hap [11]. In addition, these agents can play good role in enhancing the magnetic properties of the product.

Magnetic-nanoparticles are used in bio-applications are usually made from biocompatible materials such as magnetite (Fe_3O_4) for which susceptibility is large. These particles have to be integrated into structure of HAp thus it has the potential to achieve localized tumor heating without any side effects i.e.; hyperthermia effects. One of the main biomedicine sciences is the hyperthermia application consists of targeting magnetic nanoparticles to tumor tissue followed by application of an external alternating magnetic field. The temperature in tumor tissue is increased to above 43°C, which causes necrosis of cancer cells, but does not damage surrounding normal tissue [12]. Magnetic hydroxyapatites containing Fe or Mn or both were previously studied to form composite materials [13,14].

Nanoparticles are incorporated into different materials such as polymers, noble metals, metal oxides and silica. Many researchers have developed different magnetic nanoparticles of ferromagnetic bioglass ceramics which provide magnetic properties for hyperthermia purposes [15].

It was reported that insertion of the spinel ferrite $MnFe_2O_4$ through a wet chemistry process resulted in nanoparticles having a core–shell structure (in which the core was made up of the ferrite and the shell of HAp. Synthetic HAp has been successfully used in hard tissue surgery, as it is capable of undergoing bonding osteogenesis and is relatively insoluble *in vivo* [16].

Mn^{2+} containing HAp and tri calcium phosphate (TCP) were studied previously [17,18]. The motivation for the addition of Mn^{2+} ions to HAp was due to the fact that divalent Mn^{2+} has been linked to the activation of integrins which are defined as a family of receptors which mediate cellular interactions with extracellular matrix and cell surface ligands. In presence of Mn^{2+} ions, cell adhesion is promoted because the ligand affinity of integrin increases.

The aim of this study is to construct a new species of magnetic hydroxyapatites. These types are having a good degree of magnetic properties and compatibility properties. These types of hydroxyapatites contain Fe^{+3} and Mn^{+2} ions into the structure of HAp aiming to limit formation of magnetic secondary phase and able

to be manipulated in situ by magnetic forces. These new types of magnetic hydroxyapatites are good candidate to be used in hyperthermia applications. In fact, the use of magnetic stimulation in the field of tumor treatment is one of the modern trends which have received increased attention in scientific circles.
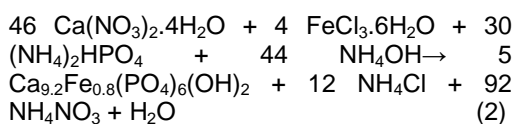
2. MATERIALS AND METHODS

2.1 Preparation of Hydroxyapatite

Analytical grades of calcium nitrate $Ca(NO_3)_2.4H_2O$ (Merck) and diammonium hydrogen phosphate $\{(NH_4)_2HPO_4\}$ (Sigma-Aldrich) with Ca/P molar ratio 1.67 were used to produce pure HAp, was produced using the following chemical reaction:

$$10(Ca(NO_3)_2.4H_2O)+6((NH_4)_2.HPO_4)+8NH_4OH \rightarrow Ca_{10}(PO_4)_6.(OH)_2+20NH_4NO_3+46H_2O \quad (1)$$
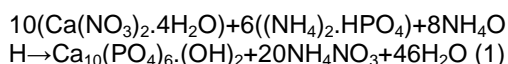
$MnCl_2.4H_2O$ (Sigma-Aldrich) and $FeCl_3.6H_2O$ (Merck) were used as sources of, Mn^{+2} and Fe^{+3} respectively. The different types of hydroxyapatites were presented in Table 1. Samples containing Mn and Fe ions are represented in equation 2 and 3. Example for $(Ca_{9.2}Fe_{0.8}(PO_4)_6(OH)_2)$ sample:

$$46 \; Ca(NO_3)_2.4H_2O + 4 \; FeCl_3.6H_2O + 30 \; (NH_4)_2HPO_4 + 44 \; NH_4OH \rightarrow 5 \; Ca_{9.2}Fe_{0.8}(PO_4)_6(OH)_2 + 12 \; NH_4Cl + 92 \; NH_4NO_3 + H_2O \quad (2)$$

and sample : $(Ca_{9.2}Mn_{0.8}(PO_4)_6(OH)_2)$

$$46 \; Ca(NO_3)_2.4H_2O + 4 \; MnCl_2.4H_2O + 30 \; (NH_4)_2HPO_4 + 40 \; NH_4OH \rightarrow 5 \; Ca_{9.2}Mn_{0.8}(PO_4)_6(OH)_2 + 8 \; NH_4Cl + 92 \; NH_4NO_3 + H_2O \quad (3)$$
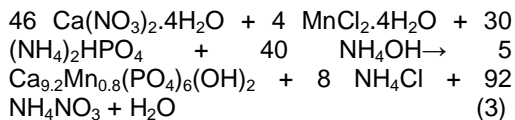
Table 1. Chemical formulas and symbols for prepared samples

	Chemical Formula	Symbol
	$Ca_{10}(PO_4)_6.(OH)_2$	HAp
Group (A)	$Ca_{9.2}Fe_{0.8}(PO_4)_6(OH)_2$	$Fe_{0.8}$- HAp
	$Ca_{8.4}Fe_{1.6}(PO_4)_6(OH)_2$	$Fe_{1.6}$- HAp
	$Ca_{7.6}Fe_{2.4}(PO_4)_6(OH)_2$	$Fe_{2.4}$- HAp
	$Ca_{6.8}Fe_{3.2}(PO_4)_6(OH)_2$	$Fe_{3.2}$- HAp
Group (B)	$Ca_{9.2}Mn_{0.8}(PO_4)_6(OH)_2$	$Mn_{0.8}$- HAp
	$Ca_{8.4}Mn_{1.6}(PO_4)_6(OH)_2$	$Mn_{1.6}$- HAp
	$Ca_{7.6}Mn_{2.4}(PO_4)_6(OH)_2$	$Mn_{2.4}$- HAp
	$Ca_{6.8}Mn_{3.2}(PO_4)_6(OH)_2$	$Mn_{3.2}$- HAp

To produce a pure hydroxyapatite sample, a calculated amount of calcium nitrate $(Ca(NO_3)_2.4H_2O)$ was dissolved in 1 L distilled water with vigorous stirring (1 h) to form 0.5 M/L. then, calculated amount of diammonium hydrogen phosphate $\{(NH_4)_2.HPO_4\}$ was also dissolved in 1 L distilled water with vigorous stirring (1 h) to form 0.5 M/L and added drop wise to the calcium nitrate, the pH of the solution was adjusted to 9 using ammonia solution. The two solutions were mixed to obtain a Ca/P molar ration of 1.667 at a controlled constant pH of about 10-11. The mixture was continuously stirred about 1 hr at temperature 80°C, until a white transparent gel was obtained. The gel was cooled and incubating at 37°C for 24 h until a white precipitate was produced. The precipitate was decanted and filtrated under vacuum by using sintered Buchner funnel with continued washing by distilled water to remove ammonia solution and then dried in oven at 90°C. The powdered sample was sintered at 10°C/min at temperatures 500, 600, 700, 800 and 900°C for 1 h then placed in air-cooling to ambient temperature. The sintered product was crushed using agate mortar and pestle to obtain resultant powder.

2.2 FTIR Measurements

Fourier transform infrared absorption signals of the studied HAp samples were measured at room temperature (20°C) in the wavelength range 4000-400 cm^{-1} using a computerized recording FTIR spectrometer (Mattson5000, USA). Fine powdered samples were mixed with KBr in the ratio 1:100 for quantitative analysis and the weighed mixtures were subjected to a load of 5t/cm^2 in an sample cell i.e to produce clear homogenous discs. Then, the IR absorption spectra were immediately measured after preparing the discs to avoid moisture attack.

2.3 X-ray Diffraction Analysis

The structure of dried and calcined samples was assessed using an X-ray powder diffractometer (a Philips PW1390 X-ray diffractometer) with Cu Kα target (Ni filter), wavelength (λ) = 1.54 Å. C/S= 1 x 10^3, KV = 40, time constant (T.C) = 2 and mA = 25 was used. The Bragg's angle (2θ) in the range of 4–70°, step size = 0.02 and step time 0.4s at room temperature. Crystallographic identification of the phases of synthesized apatites was accomplished by comparing the experimental XRD patterns to standards

complied by the Joint Committee on Powder Diffraction Standards (JCPDS).

The size of the crystallites responsible for the Bragg reflection of the (002) and (300) planes were determined using Scherer equation:

$$d = \frac{K\lambda}{\beta \cos \theta} \qquad (4)$$

where d is the crystalline diameter in nm, β is the peak width at half-maximum peak height in radians, λ is the x-ray wavelength, typically 1.54 Å, and θ is the Bragg angle.

2.4 Differential Scanning Calorimetry and Thermogravimetric Analysis

DSC/TG analysis was carried out using a NETZSCH STA 409C/CD instrument. Known mass (≈30 mg) of crushed samples was placed into an aluminum pan then sealed with a crimped lid and heated from 25°C to 1000°C at a rate of 5°C/min with argon as carrier gas at a flow rate of 30 cm^3/min.

3. RESULTS AND DISCUSSION

Calcium phosphate ceramics, particularly those with Ca/P ratios between 1.5 and 1.67, i.e., tricalcium phosphate ($Ca_3(PO_4)_2$) and stoichiometric calcium hydroxyapatite ($Ca_{10}(PO_4)_6(OH)_2$), respectively, have long been used as prime candidate biomaterials to restore, reconstruct, and replace human bone tissues [19-23]. This is because of their close chemical similarity to minerals found in calcified tissues, such as bone, tooth enamel and dentine, in both humans and vertebrates. Hydroxyapatite (HAp) is one of the most important calcium phosphates and has received wide attention as bone substitutes over the past few decades [19,24-26].

Fig. 1 shows the thermogram of the synthesized pure hydroxyapatite material. The figure reveals four distinct stages of decomposition. The first stage that occurs between 35 and 110°C is due to loss of adsorbed water with the value about (5.5% ≈ 0.0956 mg). The second stage for weight loss that occurs between 110 and 220°C is assigned to the decomposition of ammonia (5.43% ≈ 0.094 mg). The third stage is due to the dehydration of $Ca(OH)_2$ into CaO also contributes the total weight loss in this stage is 7.9% ≈ 0.13 mg. The fourth weight loss that

occurs between 300 and 700°C is due to the decomposition of nitrate is about (4.37% ≈ 0.075 mg). This temperature range for nitrate decomposition was also reported by Liu et al. [27,28]. From the thermogram presented in Fig. 1, it can deduce that temperature between 500- 900°C is a convenient for sintering process.
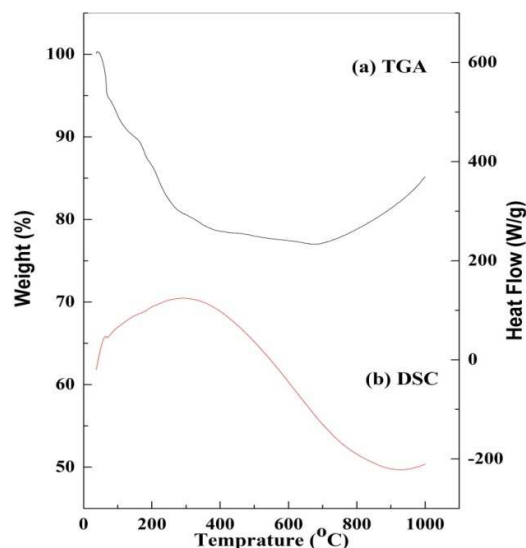

Fig. 1. DSC and TGA curves of synthesized pure hydroxyapatite material

Fig. 2 shows the XRD patterns of heat treated samples at 700°C (Plot A) and at 900°C (Plot B) for 1 h. It can be noted from this figure that amorphous hump is limited and it can't be detected. This indicates that the prepared sample has crystalline structure and the measured degree of crystallinity is 41.4%. On the other hand, the crystalline-structure peaks become sharper in the sample sintered at, 900°C resulting in crystallinity of 55.56%. Increasing degree of crystallinity to 55.56% with increasing temperature, may lead to conclude that any initial amorphous matrix present in sample is well crystallized by the effect of heat treatment. The angular location and intensity in Fig. 2 of nearly all the peaks in sample sintered at 700°C closely match the standard JCPDF database (70-0364), which indicates that the major crystalline phases are tricalcium phosphate $Ca_3(PO_4)_2$ (JCPDS 70-0364) with percentage (21.2%) besides, some extra XRD peaks can be observed in Fig. 2 that match the standard of HAp $Ca_{10}(PO_4)_6(OH)_2$ (JCPDS 72-1243) crystalline apatite phases percentage (78.8%). Then both hydroxyapatite (HAp) and calcium phosphate crystalline phases could be formed by the effect of the heat

treatment process. These phases are considered the essential phases required for bone construction.

3.1 FTIR Spectroscopic Analysis

FTIR of the as-prepared derived at 100°C HAp is shown in Fig. 3a. The figure reveals the amorphous nature of the materials since there are no characteristic sharp peaks in the spectrum. This gel is then dried and fired at temperature ranges from ≈ 500 to 900°C which helps it to convert slowly to crystalline hydroxyapatite phase with Ca/P ratio ≈ 1.67 [29]. All hydroxyapatite characteristic bands are shown clearly in Fig. 3(b-f).
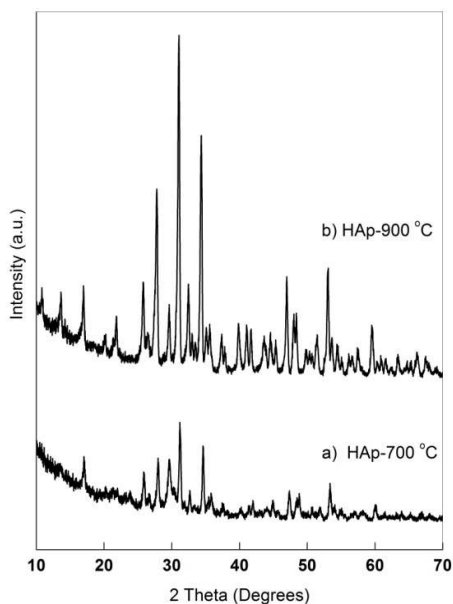

Fig. 2. XRD patterns of heat treated hydroxyapatite samples at 700°C (Plot A) and at 900°C (Plot B) for 2 h

Figure 3a shows an FTIR spectrum of the material derived at 100°C. The broad envelope between 2700 and 3700 cm^{-1} is attributed to the OH stretch of $Ca(OH)_2$, and HAp, and NH stretch of NH_4^+. The peak at 1763 cm^{-1} is assigned to N=O stretch of NO_3^-. The bending mode of H_2O is observed at 1631 cm^{-1}. The intense peak at 1382 cm^{-1} is assigned to N–O stretch of NO_3^-. The PO_4^{2-} stretching mode is positioned at 1031 cm^{-1}. The other bending modes of PO_4^{2-} are observe at 603 and 566 cm^{-1}. The sharp peak at 825 cm^{-1} is also assigned to NO_3^- bending mode.

For sample sintered at 500 to 900°C, the broad envelope observed in the above spectrum between 2700 and 3700 cm^{-1} indicates the complete loss of water, dehydration of $Ca(OH)_2$, and decomposition of NH_4^+. The peaks in the lower energy region include peaks due to PO_4^{2-} mode at 985, 1027, 1062 and 579 cm^{-1}, and that due to amorphous calcium phosphate at 1165, 1124, 757 and 579 cm^{-1} (common in PO_4^{2-} mode). Further, there is no peak corresponding to NO_3^- in this spectrum. FTIR spectrum of the sample sintered at temperature greater than 1000°C does not show any peak corresponding to that of HAp. This further confirms the XRD findings that the HAp is completely transformed to a well crystallized HAp. A similar observation was reported by for the samples calcined at 900°C [30-35]. These assignments were summarized in the Table 2.
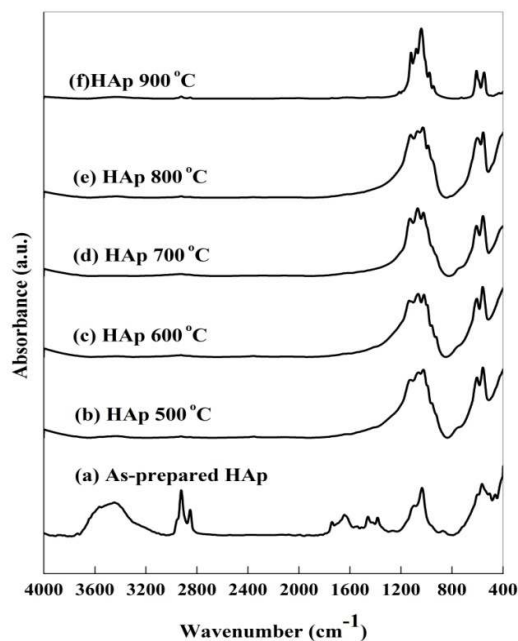

Fig. 3. FTIR of pure as-prepared hydroxyapatite (HAp) and heat treated at different temperatures

The asymmetric stretching (v_3) modes of PO_4^{-3} ions were detected at 1040, and 1092 cm^{-1} and bending mode (v_4) at 601, 575 and 561 cm^{-1} [36]. Symmetrical stretching modes of PO_4^{-3} ions v_1 and v_2 were also found at around 960 and 470 cm^{-1}, respectively [37]. Stretching modes of the hydroxyl group (OH–) were detected at around 3570 and 1630 cm^{-1} respectively [38].

3.2 FTIR Spectra of Hydroxyapatite Doped with Fe

Figs. 4.1b-e show hydroxyapatites doped with different concentrations of Fe atoms at the expense of calcium atoms with the stoichiometric ratio of (Ca+metal)/P=1.667. The figure reveals some few structural changes that may be attributed to incorporation of metal ions in hydroxyapatite structure. In Figs. 4.2b-e, the peaks in wavenumber range 500 to 700 cm^{-1} are now merged and become a broad peak rather than splitting in pure. There is an increase in the intensity of the peak at 720 cm^{-1} and the envelope in the range of 800 to 1300 cm^{-1} becomes broader; this may also be attributed to bonding of Fe to HAp structure [39]. The sharpness of vibrational peaks at 972 cm^{-1}, 1160 cm^{-1} in hydroxyapatite decreases and the peaks become broader and less intense. The absence of the sharp vibrational peaks at 940 cm^{-1}, 1110 cm^{-1}, and 1178 cm^{-1} may also be seen. Additional bands of low intensities are visible at 818 cm^{-1} and 833 cm^{-1}. These bands can be assigned to v_1 and v_3 vibrations of Fe_3O_4 groups.

Table 2. Assignments for pure HAp calcined at different temperatures

Assignments	Wavenumber (cm^{-1})
OH stretch and NH stretch of NH_4^+	2700-3700
N=O stretch of NO_3^-	1760 and 830
Bending mode of H2O	1630
N-O stretch of NO_3^-	1380
$P_2O_7^{4-}$ stretching modes	1160, 1120 and 750
PO_4^{3-} stretching modes	1060 and 1030
PO_4^{3-} bending modes	1032,1060 and 560
Common for $P_2O_7^{4-}$ and PO_4^{3-}	580

Clearly the characteristic band positions observed for both of the synthesized samples are in good agreement with that of pure HAp. This observation supported the formation of the expected cation-substituted HAp within the present experimental protocol.

3.3 XRD of the Pure Hydroxyapatite

Figure 5 shows XRD for pure HAp. The majority of peaks are indexed to the hexagonal lattice of $Ca_{10}(PO_4)_6(OH)_2$ crystal while other peaks are indexed for β-calcium phosphate (β-$Ca_3(PO_4)_2$). The wide and high peaks reveal that the pure HAp has a very small size (nanoparticles), also excellent crystal quality and no impurities were

detected by X-ray. The d-spacing, intensities and lattice parameters for the hexagonal HAp are compared with JCPDS Card (data file No. 72-1243) standard for HAp. The obtained lattice parameters are (a=9.432 and c=6.881) and the d- values of the strongest three lines are 2.81, 2.72 and 2.78.
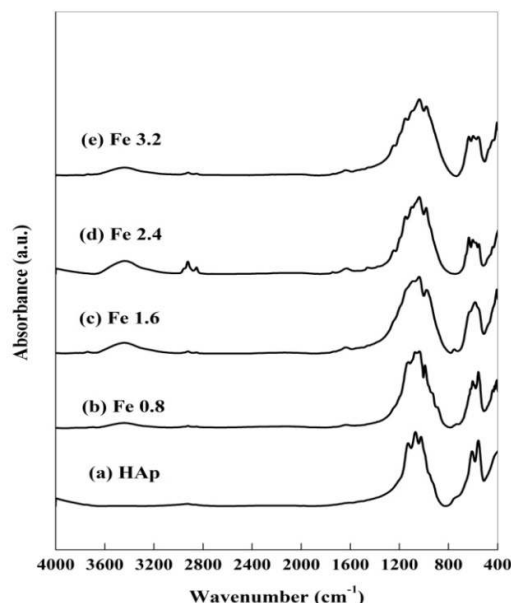

Fig. 4.1. FTIR of (a) pure hydroxyapatite HAp and (b-e) Hydroxyapatite doped with concentrations of Fe ions
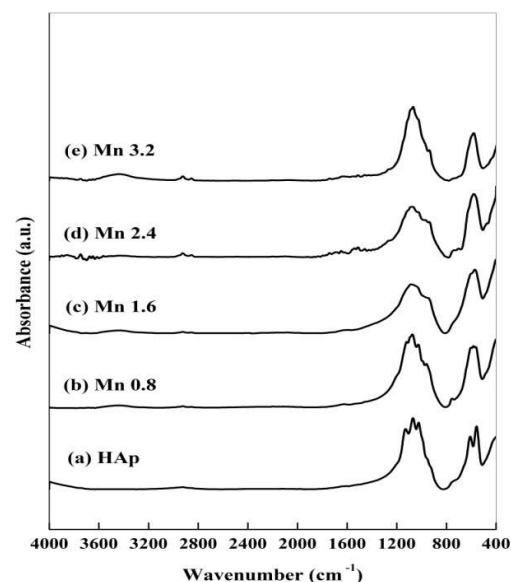

Fig. 4.2. FTIR of (a) pure hydroxyapatite HAp and (b-e) Hydroxyapatite doped with concentrations of Mn ions

3.4 XRD of Pure HAp and Fe Doped Hydroxyapatites

Fig. 6 shows XRD patterns of all samples HAp and hydroxyapatite doped with concentrations of Fe atoms. The peak positions are not clearly changed, but the peaks intensity changed and thus the degree of crystallization is changed gradually. Clearly a number of prominent peaks for apatite phase were in the XRD pattern. However, the observed intensity and d-spacing values for both the samples are in excellent agreement with the JCPDS standard data for HAp.

The amount of Fe added to the basic hydroxyapatite changes the basic structural unit and lowers the degree of crystallinity by the formation of newly crystalline phases. These phases are magnetite (Fe_3O_4) iron oxide, ICSD file no. 89-0951, cubic with lattice parameters (a=8.491) in case of samples (b-e), and calcium iron hydro-phosphate $Ca_9FeH(PO_4)_7$ ICSD file no. 89-0513 cubic phase with lattice parameters (a=10.33Å and c=37.125Å).

3.5 XRD of Pure HAp and Mn Doped Hydroxyapatites

The XRD spectrum of the Mn-doped apatite [Fig. 7 (b-e)] shows the presence of amorphous phase which supports the observed FTIR data. The reason of this nature is the temperature effect. It is well established that the degree of crystallinity increases with the increase of sintering temperature resulting several distinct peaks.

XRD patterns of all samples HAp, Hydroxyapatite doped with concentrations of Mn atoms showed that peaks present agree well with ICSD file no. 72-1243 which is hexagonal hydroxyapatite and the patterns displayed extra peaks.

The amount of manganese added distorted the structure unit of HAp and lower the degree of crystallinity to some extent and formation of a newly crystalline phases. These phases are manganese oxide (β-Mn_3O_4)ICSD file no. 89-4887, orthorhombic one with lattice parameters (a=9.55, b=9.79, and c=3.02), and calcium manganese hydro-phosphate ($Ca_9MnH(PO_4)_7$)ICSD file no. 70-0009. Also, it can be noted that lines corresponding to crystalline phases of other calcium-phosphate–based compounds are also present.

The crystallite size, crystallinity index and lattice parameters of doped and calcined (at 700℃) samples were calculated as described previously. The calculated values are tabulated in Table 3.

The lattice parameters and cell volume values of the Fe-HAp and Mn- HAp did not significantly change as compared to those of pure HAp.
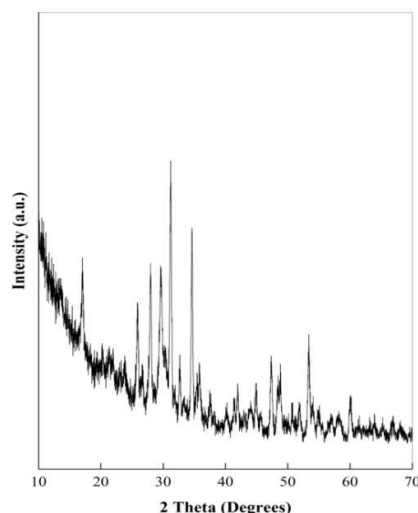

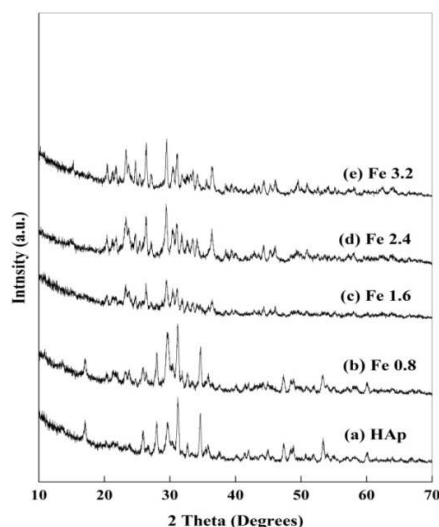**Fig. 5. XRD of pure hydroxyapatite**

Fig. 6. XRD of (a) pure hydroxyapatite HAp and (b-e) Hydroxyapatite doped with concentrations of Fe ions

An increase of the a-axis and a decrease of c-axis were detected as expected in the case of Ca substitution with ion species having a lower

radius. This observation confirmed the formation of Fe-HAp and Mn-HAp substituted apatite of hexagonal structure and conclusively proved that a variety of substitutions of both cationic and anionic is possible in hydroxyapatite structure without any significant modification of its hexagonal system.
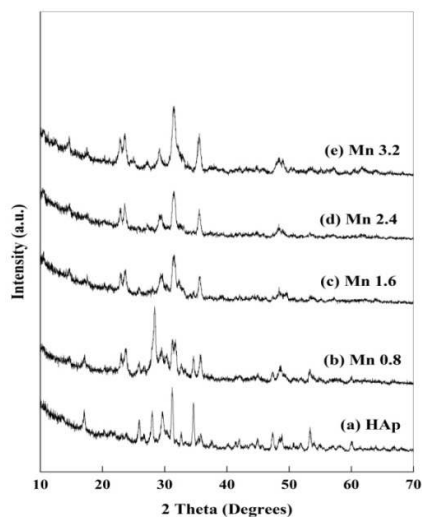

Fig. 7. XRD of (a) pure hydroxyapatite HAp and (b-e) Hydroxyapatite doped with concentrations of Mn ions

However for both cases lower values of crystallite size and crystallinity were observed as substitution significantly reduces the crystallite size as well as crystallinity. Possibly, the changes in cell volume for the latter case would be due to the substitution of more cation.

3.6 Electron Paramagnetic Resonance

It is well known that the total magnetic field of each ion is established from the spin-spin interaction of neighboring paramagnetic ions [40]. The spin-spin interaction caused by small magnetic fields and this play an important role to alter the total magnetic field of each ion. So, the energy levels of the unpaired electrons to be shifted which led to a variation of energies resulting in a broadened EPR signal.

In Fe-HAp sample, the broad feature in the g-value of 2.0 regions is attributed to separation of ferric oxide phases with different content in iron cations (Fe^{2+} and Fe^{3+}), and their separation results presence of surface oxyhydroxides and Fe-O-Fe clusters [41]. The presence of high concentration of Fe^{3+} caused electron spin-spin interactions between neighboring Fe^{3+} nuclei which yielded the broad signal. The poor crystallinity with sample Fe-HAp that results from the Fe-phosphates and Fe-oxyhydroxides would be expected to have a high concentration of neighboring Fe^{+3} ions. These agree well with results of XRD and FTIR results. The rhombic crystal field symmetry assigned to Fe-HAp suggested that Fe was occupying the rhombic Ca(2) site and not the axial Ca(1) site. However, charge compensation from Fe^{+3} substituting for Ca^{+2} could cause asymmetry distortion and lead to a rhombic environment in the Ca(1) site.

The number and position of EPR transitions for isolated Fe^{3+} ions in a site of well-defined symmetry observable in a powder spectrum depends sensitively on the local ligand-field symmetry of the sites and possible magnetic interactions between them. In the presence of a rhombic distortion of the ligand-field the g values of the three doublets of the S = 5/2 system change as a zero-field splitting parameters depending of its value it becomes possible to observe ESR signal arising from the ±3/2 and ±5/2 doublet of the excited states. Iron (III) rhombic crystal field symmetry may indicate substitution into either of the Ca sites in Fe-HAp.

Table 3. Crystallite size, degree of crystallinity and lattice parameters for pure HAp and HAp doped with Fe atoms

| Symbol	Crystallite size	Degree of crystallinity	Lattice parameters	
HAp	37.63768	41.42%	a=9.420Å	c=6.881 Å
Fe $_{0.8}$- HAp	41.41286	39.88%	a=9.392 Å	c=6.870 Å
Fe $_{1.6}$- HAp	34.46734	46.44%	a=9.434 Å	c=6.869 Å
Fe $_{2.4}$- HAp	34.46303	46.86%	a=9.441 Å	c=6.873 Å
Fe $_{3.2}$- HAp	31.8164	46.84%	a=9.443 Å	c=6.872 Å
Mn $_{0.8}$- HAp	31.85732	48.21%	a=9.392 Å	c=6.870 Å
Mn $_{1.6}$- HAp	34.49934	40.03%	a=9.444 Å	c=6.869 Å
Mn $_{2.4}$- HAp	(No Peak at 25.8)	38.97%	a=9.421 Å	c=6.853 Å
Mn $_{3.2}$- HAp	(No Peak at 25.8)	26.92%	a=9.423 Å	c=6.862 Å
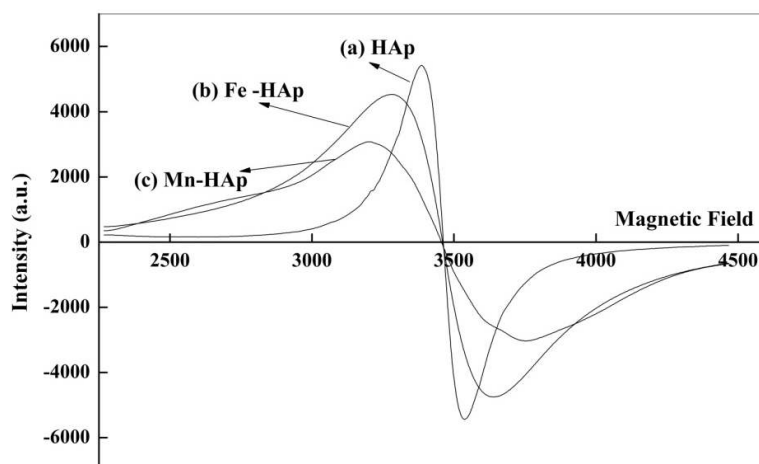
Fig. 8. EPR of pure hydroxyapatite, Fe- doped and Mn-doped hydroxyapatites

Manganese (IV) may be the cause of the low field X-band hyperfine patterns. Manganese (IV) would have originated from Mn^{+2} oxidation during Mn-HAp synthesis. However, the pink color of the Mn-HAp materials indicated that Mn^{+2} was the dominant oxidation state in the g-value = 2 [42].

The hyperfine lines of the Mn-HAp were barely detectable. Minor spectral differences were observed between the Mn-HAp and Fe-HAp showed a marked decrease in peak intensity relative to standard HAp.

The large decrease of the Mn-HAp g-value = 2.01 peak indicated that nonstructural Mn phase(s) such as poorly crystalline Mn-oxyhydroxide and Mn-phosphate phase(s) associated with the SHA crystallites [43]. Poorly crystalline Mn phase(s) also explain the broad g-value 2.01 peak in Mn-HAp that was superimposed on the hyperfine pattern because Mn^{+2} would be closely associated with one another leading to spin-spin interactions.

The central sharp peak observed in Mn-HAp and was possibly from a small concentration of an inorganic or organic contaminant in the synthesis reagents. The high intensity of the Mn^{+2} peaks Mn-HAp dominated the spectrum and masked any contamination peak. Spin-spin exchange interactions because of Mn and Cu atoms were the cause of an increase of signal broadening [44]. The entire Fe-HAp spectrum was superimposed on the broad signal that suggested the presence of sites with strong spin-spin interactions caused by poorly crystalline Fe-oxyhydroxide or Fe-phosphate phase(s).

The crystalline structure has been determined using X-ray and neutron diffraction, electron diffraction patterns of HA single crystal are not readily obtained. Its single crystal pattern of the (001) zone is especially valuable because it reveals the features of its apatite structure.

4. CONCLUSION

Nano-sized particles of pure HAp and various Fe and Mn atoms doped HAp powders have been successfully prepared via a wet chemical method. Heating the hydroxyapatite thermally results in increasing the crystallinity of prepared samples. Doping of Fe into HAp powders has greatly influenced the structure in a trend that the crystallinity was decreased with Fe and Mn atoms substitution. Good agreement with FTIR results were obtained where the splitting of band in wavenumber range 500-700 cm^{-1} is decreased up on addition of different metal ions in substitution of calcium ions. The data obtained from XRD for different powder samples were found to be in a good agreement with that obtained from FTIR. The magnetic properties from ESR results played a vital role to enhance the bioactivity and physiochemical properties of the apatite.

COMPETING INTERESTS

Authors have declared that no competing interests exist.

REFERENCES

1.   Nudelman F, Pieterse K, George A, Bomans PH, Friedrich H, Brylka LJ, et al.

The role of collagen in bone apatite formation in the presence of hydroxyapatite nucleation inhibitors. Nature Materials. 2010;9:1004-9.

2. Swetha M, Sahithi K, Moorthi A, Srinivasan N, Ramasamy K, Selvamurugan N. Biocomposites containing natural polymers and hydroxyapatite for bone tissue engineering. International Journal of Biological Macromolecules. 2010;47:1-4.

3. Zhou H, Lee J. Nanoscale hydroxyapatite particles for bone tissue engineering. Acta Biomaterialia. 2011;7:2769-81.

4. LeGeros RZ, Ito A, Ishikawa K, Sakae T, LeGeros JP. Fundamentals of hydroxyapatite and related calcium phosphates. Advanced Biomaterials: Fundamentals, Processing, and Applications. 2010;19-52.

5. Gergely G, Wéber F, Lukács I, Tóth AL, Horváth ZE, Mihály J, et al. Preparation and characterization of hydroxyapatite from eggshell. Ceramics International. 2010;36:803-6.

6. Uskoković V, Uskoković DP. Nanosized hydroxyapatite and other calcium phosphates: Chemistry of formation and application as drug and gene delivery agents. Journal of Biomedical Materials Research Part B: Applied Biomaterials. 2011;96:152-91.

7. Sadat-Shojai M, Atai M, Nodehi A, Khanlar LN. Hydroxyapatite nanorods as novel fillers for improving the properties of dental adhesives: Synthesis and application. Dental Materials. 2010;26:471-82.

8. Li M, Wang Y, Liu Q, Li Q, Cheng Y, Zheng Y, et al. In situ synthesis and biocompatibility of nano hydroxyapatite on pristine and chitosan functionalized graphene oxide. Journal of Materials Chemistry B. 2013;1:475-84.

9. Chen Y, Huang Z, Li X, Li S, Zhou Z, Zhang Y, et al. In vitro biocompatibility and osteoblast differentiation of an injectable chitosan / nano-hydroxyapatite / collagen scaffold. Journal of Nanomaterials. 2012;2012:3.

10. Maxian SH, Zawadsky JP, Dunn MG. In vitro evaluation of amorphous calcium phosphate and poorly crystallized hydroxyapatite coatings on titanium implants. Journal of Biomedical Materials Research. 1993;27:111-7.

11. Kane RJ, Roeder RK. Effects of hydroxyapatite reinforcement on the architecture and mechanical properties of freeze-dried collagen scaffolds. Journal of the Mechanical Behavior of Biomedical Materials. 2012;7:41-9.

12. Neuwelt EA, Várallyay CG, Manninger S, Solymosi D, Haluska M, Hunt MA, et al. The potential of ferumoxytol nanoparticle magnetic resonance imaging, perfusion, and angiography in central nervous system malignancy: A pilot study. Neurosurgery. 2007;60:601-12.

13. Reddy LH, Arias JL, Nicolas J, Couvreur P. Magnetic nanoparticles: Design and characterization, toxicity and biocompatibility, pharmaceutical and biomedical applications. Chemical Reviews. 2012;112: 5818-78.

14. Ge F, Li M-M, Ye H, Zhao B-X. Effective removal of heavy metal ions Cd2+, Zn2+, Pb2+, Cu2+ from aqueous solution by polymer-modified magnetic nanoparticles. Journal of Hazardous Materials. 2012; 211:366-72.

15. Pankhurst QA, Connolly J, Jones S, Dobson J. Applications of magnetic nano-particles in biomedicine. Journal of Physics D: Applied Physics. 2003;36:R167.

16. Wei G, Ma PX. Structure and properties of nano-hydroxyapatite/polymer composite scaffolds for bone tissue engineering. Biomaterials. 2004;25:4749-57.

17. Pereira Moreira M, Teixeira da Silva Aragão V, de Almeida Soares GD, Araujo dos Santos E. Simultaneous Insertion of Mg2+, Sr2+ and Mn2+ Ions into Hydroxyapatite Structure. Key Engineering Materials. 2012;493:20-6.

18. Mayer I, Cohen S, Gdalya S, Burghaus O, Reinen D. Crystal structure and EPR study of Mn-doped β-tricalcium phosphate. Materials Research Bulletin. 2008;43:447-52.

19. Campoccia D, Montanaro L, Arciola CR. A review of the biomaterials technologies for infection-resistant surfaces. Biomaterials. 2013;34:8533-54.

20. Chen Q, Baino F, Pugno NM, Vitale-Brovarone C. Bonding strength of glass-ceramic trabecular-like coatings to ceramic substrates for prosthetic applications. Materials Science and Engineering: C. 2013;33:1530-8.

21. Garmendia N, Olalde B, Obieta I. 16 - Biomedical applications of ceramic nanocomposites. In: Banerjee R, Manna I, editors. Ceramic Nanocomposites: Woodhead Publishing. 2013;530-47.

22. Goh Y-F, Alshemary AZ, Akram M, Abdul Kadir MR, Hussain R. In vitro study of nano-sized zinc doped bioactive glass. Materials Chemistry and Physics. 2013; 137:1031-8.

23. Jones JR. Review of bioactive glass: From Hench to hybrids. Acta Biomaterialia. 2013;9:4457-86.

24. A History of Biomaterials. In: Lemons BDRSHJSE, editor. Biomaterials Science (Third Edition): Academic Press. 2013; xli-liii.

25. Chapter 20 - Dental Implants. In: Rawls KJASR, editor. Phillips' Science of Dental Materials (Twelfth Edition). St. Louis: Content Repository Only! 2013;499-518.

26. Bose S, Bandyopadhyay A. Chapter 1 - introduction to biomaterials. In: Bose AB, editor. Characterization of Biomaterials. Oxford: Academic Press. 2013;1-9.

27. Liu X, Rahaman MN, Hilmas GE, Bal BS. Mechanical properties of bioactive glass (13-93) scaffolds fabricated by robotic deposition for structural bone repair. Acta Biomaterialia. 2013;9:7025-34.

28. Liu Y, Lim J, Teoh S-H. Review: Development of clinically relevant scaffolds for vascularised bone tissue engineering. Biotechnology Advances. 2013;31:688-705.

29. Shadanbaz S, Dias GJ. Calcium phosphate coatings on magnesium alloys for biomedical applications: A review. Acta Biomaterialia. 2012;8:20-30.

30. Bellucci D, Sola A, Gazzarri M, Chiellini F, Cannillo V. A new hydroxyapatite-based biocomposite for bone replacement. Materials Science and Engineering: C. 2013;33:1091-101.

31. Grasso S, Chinnam RK, Porwal H, Boccaccini AR, Reece MJ. Low temperature spark plasma sintering of 45S5 Bioglass®. Journal of Non-Crystalline Solids. 2013;362:25-9.

32. Li HC, Wang DG, Hu JH, Chen CZ. Effect of various additives on microstructure, mechanical properties, and in vitro bioactivity of sodium oxide-calcium oxide-silica-phosphorus pentoxide glass–

ceramics. Journal of Colloid and Interface Science. 2013;405:296-304.

33. Scalera F, Gervaso F, Sanosh KP, Sannino A, Licciulli A. Influence of the calcination temperature on morphological and mechanical properties of highly porous hydroxyapatite scaffolds. Ceramics International. 2013;39:4839-46.

34. Sprio S, Guicciardi S, Dapporto M, Melandri C, Tampieri A. Synthesis and mechanical behavior of β-tricalcium phosphate/titania composites addressed to regeneration of long bone segments. Journal of the Mechanical Behavior of Biomedical Materials. 2013;17:1-10.

35. Wu Q, Zhang X, Wu B, Huang W. Effects of microwave sintering on the properties of porous hydroxyapatite scaffolds. Ceramics International. 2013;39:2389-95.

36. Chang C, Peng N, He M, Teramoto Y, Nishio Y, Zhang L. Fabrication and properties of chitin/hydroxyapatite hybrid hydrogels as scaffold nano-materials. Carbohydrate Polymers. 2013;91:7-13.

37. Shen Y, Liu J, Lin K, Zhang W. Synthesis of strontium substituted hydroxyapatite whiskers used as bioactive and mechanical reinforcement material. Materials Letters. 2012;70:76-9.

38. Rehman I, Bonfield W. Characterization of hydroxyapatite and carbonated apatite by photo acoustic FTIR spectroscopy. Journal of Materials Science: Materials in Medicine. 1997;8:1-4.

39. Sarath Chandra V, Baskar G, Suganthi R, Elayaraja K, Ahymah Joshy M, Sofi Beaula W, et al. Blood compatibility of iron-doped nanosize hydroxyapatite and its drug release. ACS Applied Materials & Interfaces. 2012;4:1200-10.

40. Desrosiers M, Schauer DA. Electron paramagnetic resonance (EPR) biodosimetry. Nuclear Instruments and Methods in Physics Research Section B: Beam Interactions with Materials and Atoms. 2001;184:219-28.

41. Jiang M, Terra J, Rossi A, Morales M, Saitovitch EB, Ellis D. Fe 2+/F e 3+ substitution in hydroxyapatite: Theory and experiment. Physical Review B. 2002;66:224107.

42. Oliveira L, Rossi A, Baffa O. A comparative thermoluminescence and electron spin resonance study of synthetic carbonated

A-type hydroxyapatite. Applied Radiation and Isotopes. 2012;70:533-7.

43. Ravindranadh K, Babu B, Manjari VP, Rao GT, Rao M, Ravikumar R. Optical and structural Properties of undoped and Mn^{2+} doped Ca-Li hydroxyapatite nanopowders using mechanochemical synthesis. Journal of Luminescence; 2014.

44. Chaikina M, Bulina N, Ishchenko A, Prosanov IY. Mechanochemical synthesis of hydroxyapatite and its modifications: Composition, structure, and properties. Russian Physics Journal. 2014;56: 1176-82.

Peer-review history:
The peer review history for this paper can be accessed here:
http://sciencedomain.org/review-history/13802